Plasmonics (2025) 20:1237–1248
https://doi.org/10.1007/s11468-024-02363-9

RESEARCH

Highly Sensitive Two-Parameter Anti-resonant Fiber (ARF) Sensor Based on Surface Plasmon Resonance in the Terahertz Band

Jie He[1] · Jianxin Wang[1] · Xili Lu[2] · Wei Liu[1] · Jingwei Lv[1] · Lin Yang[1] · Qiang Liu[1] · Paul K. Chu[3,4,5] · Chao Liu[1]

Received: 1 April 2024 / Accepted: 14 May 2024 / Published online: 27 May 2024

Abstract

A two-parameter anti-resonant fiber (ARF) sensor based on the principle of surface plasmon resonance (SPR) is designed to detect refractive index (RI) and temperature simultaneously. Graphene is coated on the externally cut negative curvature tube as the plasmonic medium to excite terahertz SPR for detecting the RI of the external liquid. In addition, polydimethylsiloxane (PDMS) is filled in the graphene-coated tube to sense the temperature of the liquid. The properties of the ARF-SPR sensor are analyzed by the finite element method. The maximum wavelength sensitivity and amplitude sensitivity of 13,888.9 μm/RIU and 87.40 RIU^{-1} respectively are observed at the second resonance peak for RIs between 1.3 and 1.36, and the minimum resolution is 7.2×10^{-9} RIU^{-1}. In the temperature range of 26.85 to 76.85 °C, the first resonance peak is insensitive to the temperature, and the maximum temperature sensitivity and amplitude sensitivity of the second resonance peak are 8.4 μm/°C and 0.058 $°C^{-1}$, respectively, with a resolution on the order of 10^{-5}. This special design, boasting a simple structure, overcomes the limitations of single-parameter measurements and solves the problems of two-parameter cross-sensitivity while offering excellent sensing performance.

Keywords Surface plasmon resonance · Anti-resonant fibers · Two-parameter · Graphene

Introduction

The photonic crystal fiber (PCF) taking advantage of the surface plasmon resonance (SPR) phenomenon can dramatically improve the performance of fiber optic sensors such as an ultra-wide sensing range, controllable resonance wavelengths, and high-precision detection [1–7]. SPR is the absorption of incident light energy by free electrons in a metal to produce collective oscillations, resulting in energy loss. SPR technology has the advantages of fast response, real-time dynamic monitoring, label-free detection, and no sample damage. It has been applied to measure biomedical analytes, hazardous chemicals, and environmental pollutants [8, 9]. Previous efforts have mainly focused on the visible and near-infrared spectra, and metals like gold and silver are typically chosen to excite SPR due to the large number of conducting electrons in the metals [10–13]. The terahertz (THz) range of 0.1–10 THz is between the near-infrared and microwave regions. Owing to the unique spectral location, it offers advantages not available at other wavelengths, for instance, broad bandwidth, low photon energy, and high penetrability [14]. Compared to visible light, THz waves can penetrate opaque biological samples non-destructively and are compatible with the vibrational and rotational energy levels of biological macromolecules, consequently enabling non-invasive detection of biomolecules and cellular structures [15]. However, gold and silver cannot excite THz SPR due to the low energy of THz waves, which can be absorbed by almost all optical materials. It has been found that some 2D and polymer materials exhibit relatively low absorption of terahertz waves in the broadband spectral region. For example, Wang et al. [16] have designed a PCF with

✉ Chao Liu
msm-liu@126.com

1 School of Physics and Electronic Engineering, Northeast Petroleum University, Daqing 163318, China

2 School of Materials Science and Chemical Engineering, Harbin Engineering University, Harbin 150001, China

3 Department of Physics, City University of Hong Kong, Tat Chee Avenue, Kowloon, Hong Kong, China

4 Department of Materials Science and Engineering, City University of Hong Kong, Tat Chee Avenue, Kowloon, Hong Kong, China

5 Department of Biomedical Engineering, City University of Hong Kong, Tat Chee Avenue, Kowloon, Hong Kong, China

graphene-coated cladding holes showing an average sensitivity of 208.14 GHz/RIU in the frequency range of 1–2.5 THz. The D-type PCF coated with graphene on the polished plane shows an average wavelength sensitivity of 305.4 μm/RIU in the 0.4–0.8 THz range. Liu et al. [17] have designed a MoS_2-based D-type PCF-SPR sensor for the terahertz band to detect blood components with a sensitivity of 715.59 μm/RIU, and Zhang et al. [18] have proposed a D-type PCF with polyvinylidene fluoride (PVDF) as the SPR medium for the THz band showing a maximum wavelength sensitivity of 335.00 μm/RIU.

Although these sensors offer certain advantages and structural improvements, the manufacturing complexity increases. Moreover, these terahertz sensors are normally limited to the detection of a single parameter. In this respect, the anti-resonant fiber (ARF) consisting of a glass tube or hyphenated tube with a certain thickness can perfectly confine light in the empty core through the anti-resonance effect in the cladding tube to reduce loss and broadening of the frequency band [19–22]. Compared with the PCF structure, there is no complex arrangement of air holes in the ARF thus simplifying the design and preparation. As aforementioned, the terahertz sensors are all limited to single parameter detection. This type of sensor is relatively difficult to produce, and it is obviously not economical if only a single parameter can be measured.

In this work, a graphene-coated ARF-SPR sensor is designed and analyzed for the detection of both the refractive index and temperature in the frequency range of 0.1–0.4 THz. The ARF consists of five groups of conjoined tubes, where graphene is selectively coated on the surface of the negative curvature tubes as the plasmonic medium to excite terahertz SPR. Furthermore, temperature-sensitive dimethylsiloxane (PDMS) is incorporated into the graphene-coated tubes to detect temperature accurately. Based on the finite element analysis and optimization, in the refractive index (RI) range of 1.30–1.36 and temperature range of 26.85–76.85 °C, the average RI sensitivity and temperature sensitivity are 9906.76 μm/RIU and 5.97 μm/°C, respectively. Meanwhile, the problem of two-parameter cross-sensitivity is overcome by constructing and deconstructing the sensing matrix.

Structure and Numerical Modeling

The ARF-SPR sensor is analyzed by the COMSOL software based on the finite element method. The 2D simulation was able to achieve theoretically optimal performance of the sensor, examine the robustness of the sensor, and increase the error-tolerance of the actual preparation. The graphene ARF-SPR depicted in Fig. 1 consists of 5 sets of conjoined tubes. The inner tube radius ratio of $\Lambda_1 = a/b$ (a and b are the long and short axes of the inner tube, respectively) is adopted to constrain the core mode and enhance SPR. The radius ratio of the outer tube is $\Lambda_2 = a_1/b_1$ (a_1 and b_1 are the long and short axes of the outer tube, respectively), which reduces the limiting loss. The radius of the cladding tube is R and the radius of the center hole core of the inner tube is R_1. The wall thickness of all the negative curvature tubes in this structure is t. When t satisfies the resonance condition expressed by Eq. (1) [23], light in the core will leak to the cladding, and the guiding mode will be unstable in long-distance transmission. Conversely, when the ARF beam does not satisfy the anti-resonance condition, the beam is confined in the empty core and

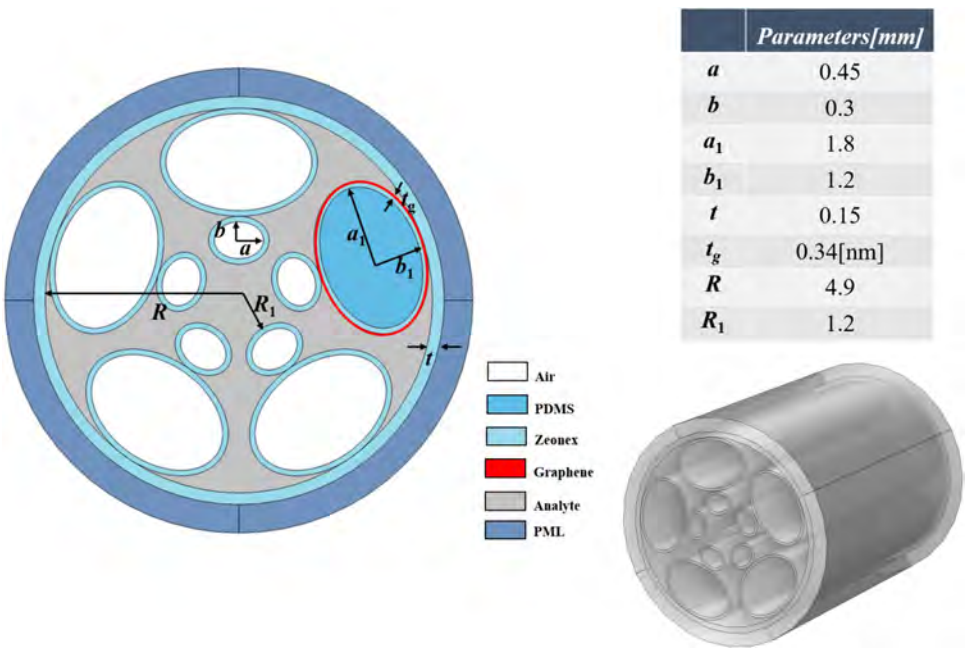

	Parameters[mm]
a	0.45
b	0.3
a_1	1.8
b_1	1.2
t	0.15
t_g	0.34[nm]
R	4.9
R_1	1.2

Fig. 1 Cross-section of the graphene ARF-SPR sensor

resonates with the graphene surface plasmon polariton (SPP) to affect SPR:

$$t = \frac{\lambda m}{2 \times \sqrt{\left(n_{\text{mat}}^2 - n_{\text{air}}^2\right)}} \tag{1}$$

where n_{mat} and n_{air} denote the RI of the material and air, respectively, m is a nonzero integer of the resonance order, λ indicates the wavelength, and t represents the thickness of the negative curvature tube. Negative curvature tubes with a thickness of t are made of the polymer Zonex, which is chosen as the substrate material because of its constant refractive index of 1.53. Zonex has low absorption loss in the terahertz range with an absorption coefficient of 0.2 cm^{-1}. Dispersion is negligible in comparison with other common fibrous materials such as SiO_2, PMMA, and Teflon [24, 25]. In order to efficiently excite SPR in the THz band, graphene is introduced as the plasmonic medium as it has superior properties such as localized electric field enhancement, low optical loss, and linear dispersion [26, 27]. The electromagnetic properties of monolayer graphene can be expressed by the 2D surface conductivity, which can be calculated by the Kubo formula [28, 29]:

$$\sigma_{2\text{D}} = \sigma_{2\text{D}}^{intra} + \sigma_{2\text{D}}^{inter} \tag{2}$$

$$\sigma_{2D}^{intra} = \frac{i\, e^2\, k_B T}{\pi \hbar^2 (\omega + i2\Gamma)} \times \left[\frac{\mu_{\text{c}}}{k_{\text{B}}\, T} + 2 \ln\left(e^{-\frac{\mu_{\text{c}}}{k_{\text{B}}\, \text{T}}} + 1 \right) \right] \tag{3}$$

$$\sigma_{2D}^{inter} = \frac{ie^2}{4\pi\hbar} \ln\left[\frac{2\,\mu_{\text{c}} - (\omega + i2\Gamma)\hbar}{2\,\mu_{\text{c}} + (\omega + i2\Gamma)\hbar} \right] \tag{4}$$

where σ_{2D}^{intra} and σ_{2D}^{inter} represent graphene interband electron migration and intraband electron migration, respectively; $\omega = 2\pi f$ is the angular frequency; μ_c, e, and $\hbar$ represent the Fermi energy, electron charge, and simplified Planck's constant, respectively; $\Gamma = 0.1\text{meV}$ stands for graphene carrier scattering rate; T is 300 K; and k_B is Boltzmann's constant. In the THz range where photon energies are low, the contribution of in-band transitions in graphene dominates, and graphene acts as a metal with Drude-like conductivity as shown by Eq. (5) [30, 31]:

$$\sigma_{intra} = i \frac{e^2\, \mu}{\pi\, \hbar^2 \left(\omega + i\, \tau^{-1}\right)} \tag{5}$$

The relative complex permittivity of graphene can be expressed by Eq. (6) [31]:

$$\varepsilon_g = 1 + \frac{i\sigma_{intra}}{\omega \varepsilon_0 t_g} \tag{6}$$

where ε_0 is the dielectric constant of the vacuum and the thickness of single-layer graphene t_g is 0.34 nm. In order for the ARF to detect both the RI and temperature, the graphene-coated tube is filled with the temperature-sensitive PDMS. In fact, both the optical fiber itself and graphene respond to temperature, but the response is insignificant. Therefore, in order to improve the temperature sensitivity of the ARF sensor, PDMS is introduced. The RI changes with temperature can be derived by Eq. (7) [32]:

$$n_{PDMS} = -4.5 \times 10^{-4} T + 1.4716 \tag{7}$$

where T is the temperature. In two-parameter sensing, in order to solve the cross-sensitivity problem caused by refractive index and temperature, the two-parameter measurement matrix of the sensor is expressed by Eq. (8) [33, 34]:

$$\begin{pmatrix} \Delta\lambda_1 \\ \Delta\lambda_2 \end{pmatrix} = \begin{pmatrix} S_1(n) & S_1(T) \\ S_2(n) & S_2(T) \end{pmatrix} \begin{pmatrix} \Delta n \\ \Delta T \end{pmatrix} \tag{8}$$

where $\Delta\lambda_1$ and $\Delta\lambda_2$ denote the resonance frequency shifts of the two resonance peaks, Δn and ΔT are the changes of RI and temperature, and $S_{\text{i}}(n)$ and $S_i(T)(i = 1, 2)$ are the RI sensitivity and temperature sensitivity of the two resonance peaks, respectively. In practical sensing, the RI and temperature are demodulated by Eq. (9) [35]:

$$\begin{pmatrix} \Delta n \\ \Delta T \end{pmatrix} = \begin{pmatrix} S_2(n) & S_1(T) \\ S_2(n) & S_2(T) \end{pmatrix}^{-1} \begin{pmatrix} \Delta\lambda_1 \\ \Delta\lambda_2 \end{pmatrix} \tag{9}$$

As shown in Fig. 1, the blue area on the outside of the ARF structure is the perfect matching layer (PML) that provides the ideal boundary conditions. The complete mesh contains 7060 domain cells and 1252 boundary cells. The initial parameters of the ARF structure are $R = 4.9$ mm, $R_1 = 1.2$ mm, $\Lambda_1 = a/b = 1.5$ mm ($a = 0.45$ mm and $b = 0.3$ mm), $\Lambda_2 = a_1/b_1 = 1.5$ mm ($a_1 = 1.8$ mm and $b_1 = 1.2$ mm), and $t = 0.15$ mm. The initial RI and temperature of the analyte are set to 1.3 and 300 K. The initial resonance curve can be obtained by calculating the confinement loss of terahertz waves in the ARF, and the loss is given by Eq. (10) [36]:

$$L = 8.686 \times \frac{2\pi}{\lambda} \times 10^7 \text{Im}\left(n_{eff}\right)(\text{dB/cm}) \tag{10}$$

where λ is the wavelength and $\text{Im}\left(n_{\text{eff}}\right)$ is the imaginary part of the effective RI of the core guide mode. The numerical results show that two independent resonance peaks are generated in the 0.1- to 0.4-THz frequency range, and the two resonance peaks are separated without a crosstalk with each other. Each resonance peak corresponds to an SPP mode. The SPP mode of peak 1 is excited by graphene in contact with the analyte, and the SPP mode of peak 2 is

excited by graphene in touch with the temperature-sensitive PDMS. These two independent SPP modes are coupled to the fiber core guiding mode, thus enabling the measurement of the analyte RI and temperature change in the range of $T = 26.85–76.85$ °C and $n_a = 1.30–1.36$. Meanwhile, in order to obtain the best performance, the ARF structure needs to be optimized. Here, the inner tube radius ratio Λ_1, outer tube radius ratio Λ_2, and tube wall thickness t are optimized sequentially from inside to outside.

The inner tube radius ratio Λ_1 is firstly optimized. Since the inner-cut negative curvature tube is closer to the orthogonal state of the core mode, the variation of Λ_1 has a larger impact on the resonance strength of the fundamental mode. Changing the size of the inner tube radius affects the effective RI, which in turn changes the ability of the core layer to confine the optical energy, thus playing a decisive role in constraining the mode field. The loss spectra for different values of Λ_1 under the initial conditions are shown in Fig. 2(a). Both resonance peaks shift significant, while the resonance frequency change of peak 1 is more significant and the loss spectrum is sharper. The SPP mode of peak 1 does not stem from the temperature-sensitive material, implying that peak 1 mainly responds to the RI change. Fig. 2b shows the peak 1 loss curves for different Λ_1 values and refractive indexes of 1.3 and 1.31. As the Λ_1 ratio decreases, the resonance frequency blueshifts. Fig. 2(c-d) show that the peak 1 resonance frequency is negatively correlated with Λ_1, and the wavelength sensitivity reaches the maximum for $\Lambda_1 = 1.3$. Therefore, $\Lambda_1 = 1.3$ (i.e., $a = 0.6$ and $b = 0.45$) is selected as the optimal inner tube radius ratio, at which the wavelength sensitivity is 5998.4 μm/RIU.

After determining the inner tube radius ratio Λ_1, the outer tube radius ratio Λ_2 is optimized. Figure 3a shows the loss spectra for different values of Λ_2. Peak 2 shifts significantly but peak 1 hardly changes. This is because the temperature-sensitive material (PDMS) is filled inside the outer tube coated with graphene, and the SPP mode of peak 2 is in direct contact with PDMS, so that the outer tube radius ratio Λ_2 mainly reflects the temperature change. Fig. 3(b) exhibits the peak 2 loss curves for different values of Λ_2 for a fixed temperature ($T = 26.85–36.85$ ℃). As Λ_2 becomes smaller, the resonant frequency red-shifts and the peak loss increases gradually. This can be explained by that as the ratio of the inner tube radius Λ_2 decreases, the core mode gets closer to the graphene, resulting in a larger contact area between the fiber core mode field and graphene coating and strong resonance between the core mode and graphene SPP mode. Fig. 3(c-d) show that the trend of the resonance frequency is inversely proportional to Λ_2. When $\Lambda_2 > 1.5$ mm, the wavelength sensitivity tends to decrease. Λ_2 is determined to be 1.5 mm (i.e., $a_1 = 1.8$ and $b_1 = 1.2$), at which the wavelength sensitivity reaches the maximum of 6.16 μm/°C.

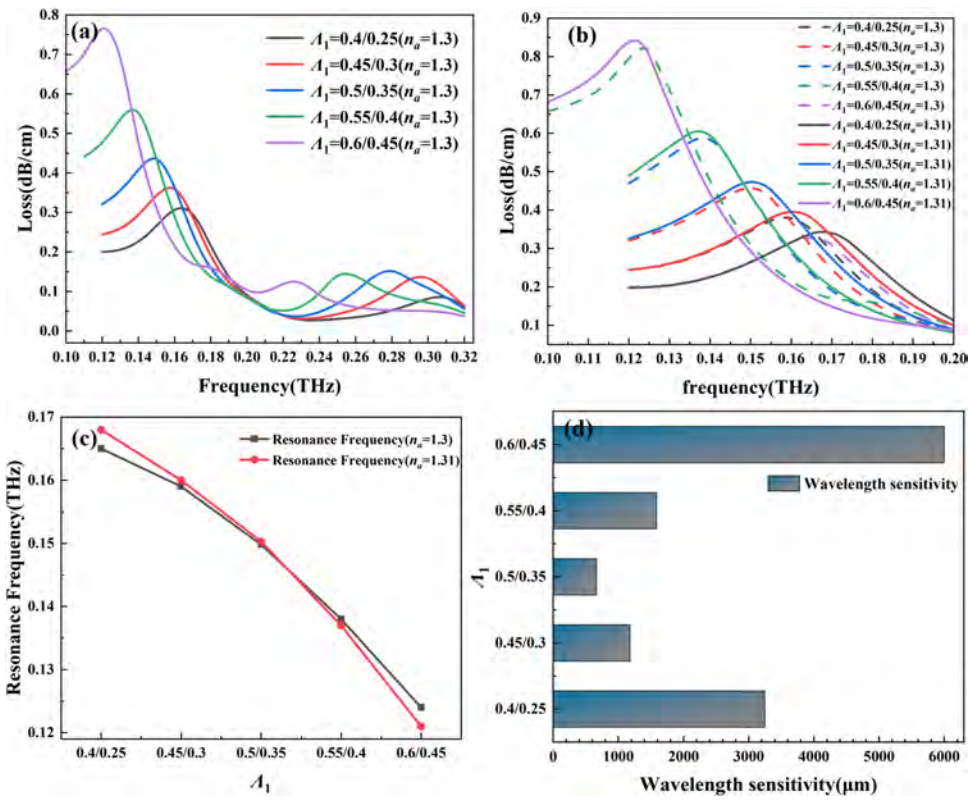

Fig. 2 **a**-**b** Loss spectra for different values of Λ_1; first resonance peaks: **c** resonant frequency and **d** wavelength sensitivity

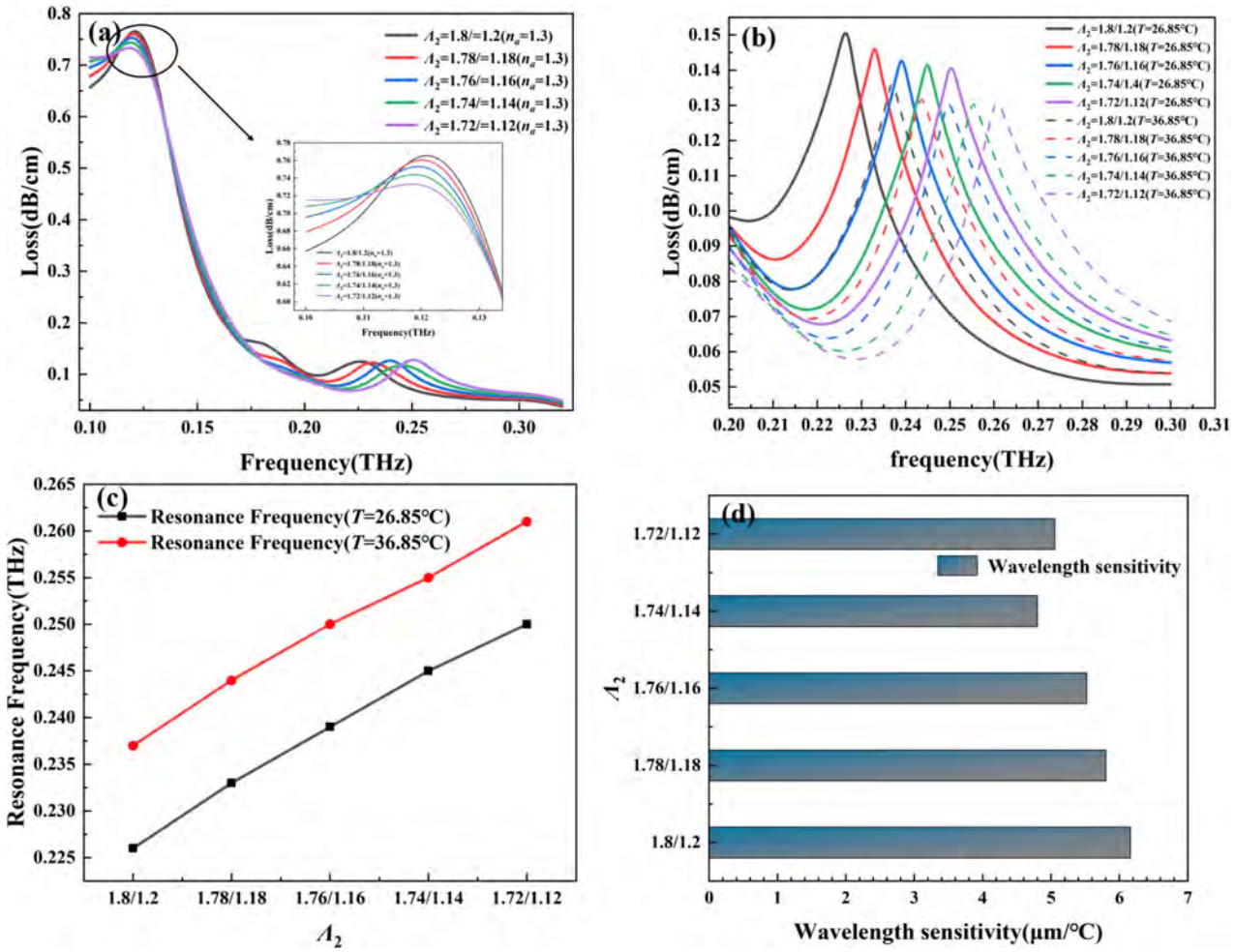

Fig. 3 **a**-**b** Loss spectra for different values of Λ_2; second resonance peak: **c** resonant frequency and **d** wavelength sensitivity

After determining the inner tube radius Λ_1 and outer tube radius Λ_2, the tube wall thickness t is optimized. As shown in Fig. 4a, the resonance frequency of the resonance peaks blueshifts with tube wall thickness, and the change of the resonance frequency of peak 1 is more significant, indicating that the change of the tube wall thickness t has a more significant influence on the RI. As shown in Fig. 4(b-c) the RI of the analyte is fixed and the tube wall thickness increases from 0.11 to 0.15. As t increases, the resonance frequency shifts to the shorter frequencies approach and the depth of loss declines. This is because as the wall thickness increases, the damping effect strengthens and coupling becomes weaker. The variation of wavelength sensitivity with frequency for different tube wall thicknesses is presented in Fig. 4d, and t = 0.14 mm gives rise to the maximum sensitivity, at which the wavelength sensitivity increases from 5998.4 to 6303.4 μm/RIU. Hence, t = 0.14 mm is selected. In summary, the optimized parameters are Λ_1 = 1.3 mm, Λ_2 = 1.5 mm, and t = 0.14 mm.

The most common commercial fiber preparation techniques are stacking and stretching, drilling, 3D printing, and so on [37–39]. Micrometer-scale node-free hollow ARFs are currently possible using stacking and stretching techniques, and complex ARF structures with nested negative curvature tubes can also be prepared by this technique [40, 41]. Therefore, using the existing stacking and stretching techniques, the proposed ARF-SPR sensors can be fabricated. High-quality graphene can be prepared by chemical vapor deposition (CVD) and oxidation/reduction described by Chen et al. [42] and Voiry et al. [43]. High-pressure CVD can be used to incorporate the temperature-sensitive materials into the negative curvature tube for the measurement of temperature [44]. The detection process of the ARF-SPR sensor is illustrated in Fig. 5a. SMFs are welded on both sides of the sensor and connected to the light source and OSA, respectively, and the data measured by the OSA are transferred to the PC to generate the loss spectra.

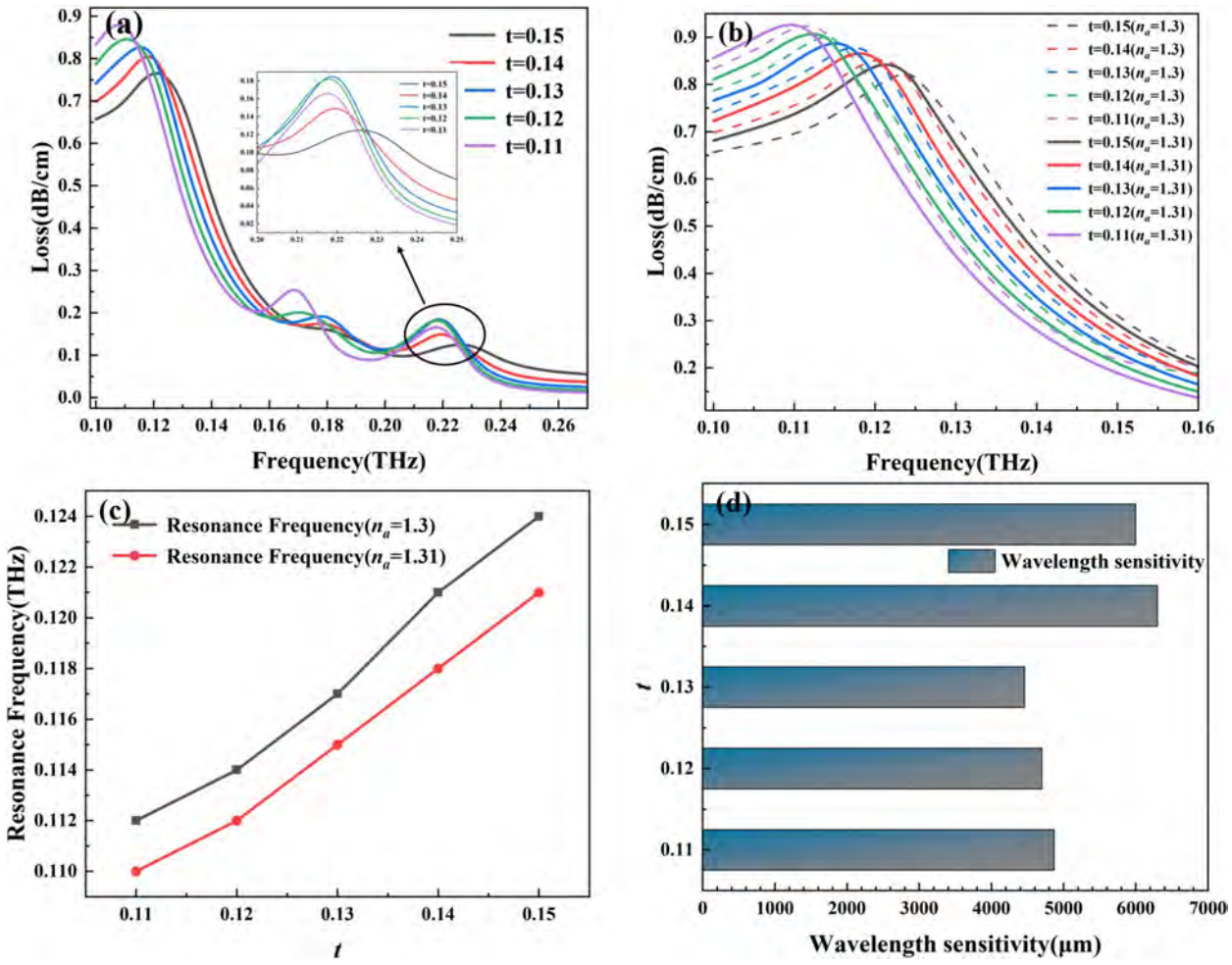

Fig. 4 **a-b** Loss spectra for different values of *t*; first resonance peak: **c** resonant frequency and **d** wavelength sensitivity

Results and Discussion

According to the full-vector finite element analysis, the coupling characteristics between the fundamental mode and SPP mode, mode field distribution, and properties of the ARF-SPR sensor are theoretically investigated.

Coupling Mechanism

The mode characteristics of the optimized sensor are determined for $n_a = 1.33$ and $T = 26.85$ ℃. Figure 5b shows the dispersion relationship between the fundamental and SPP modes. Two obvious resonance peaks are observed from the loss spectrum, and the changes of the base and SPP modes of the two resonance peaks display the same pattern, in which 0.113 THz and 0.30 THz are the resonance frequencies of the first and second resonance peaks corresponding to peak losses of 0.87 dB/cm and 0.096 dB/cm, respectively, whereas graphene exhibits very low optical loss. Figure 5c–n shows the mode field distributions of the fundamental (Fig. 5c–h) and SPP modes (Fig. 5i–n) for the two resonance peaks near the resonance frequency. In the low-frequency range, the photon energy is mainly confined inside the fiber core, and the energy is gradually transferred from the fundamental mode to the SPP mode as frequencies increase. The limiting loss peaks at the resonance frequency and the coupling strength between the base and SPP modes reach the maximum. At this time, the energy in the core region is rapidly converted into the SPP energy in the graphene surface layer, leading to the change of the effective RI of the fundamental and SPP modes. With increasing frequencies, energy is transferred from the graphene-dielectric interface back to the fiber core.

Refractive Index (RI)

The sensing characteristics of the ARF structure are evaluated based on the wavelength sensitivity. The refractive index sensitivity and temperature sensitivity are defined by Eqs. (11) [45] and (12) [46]:

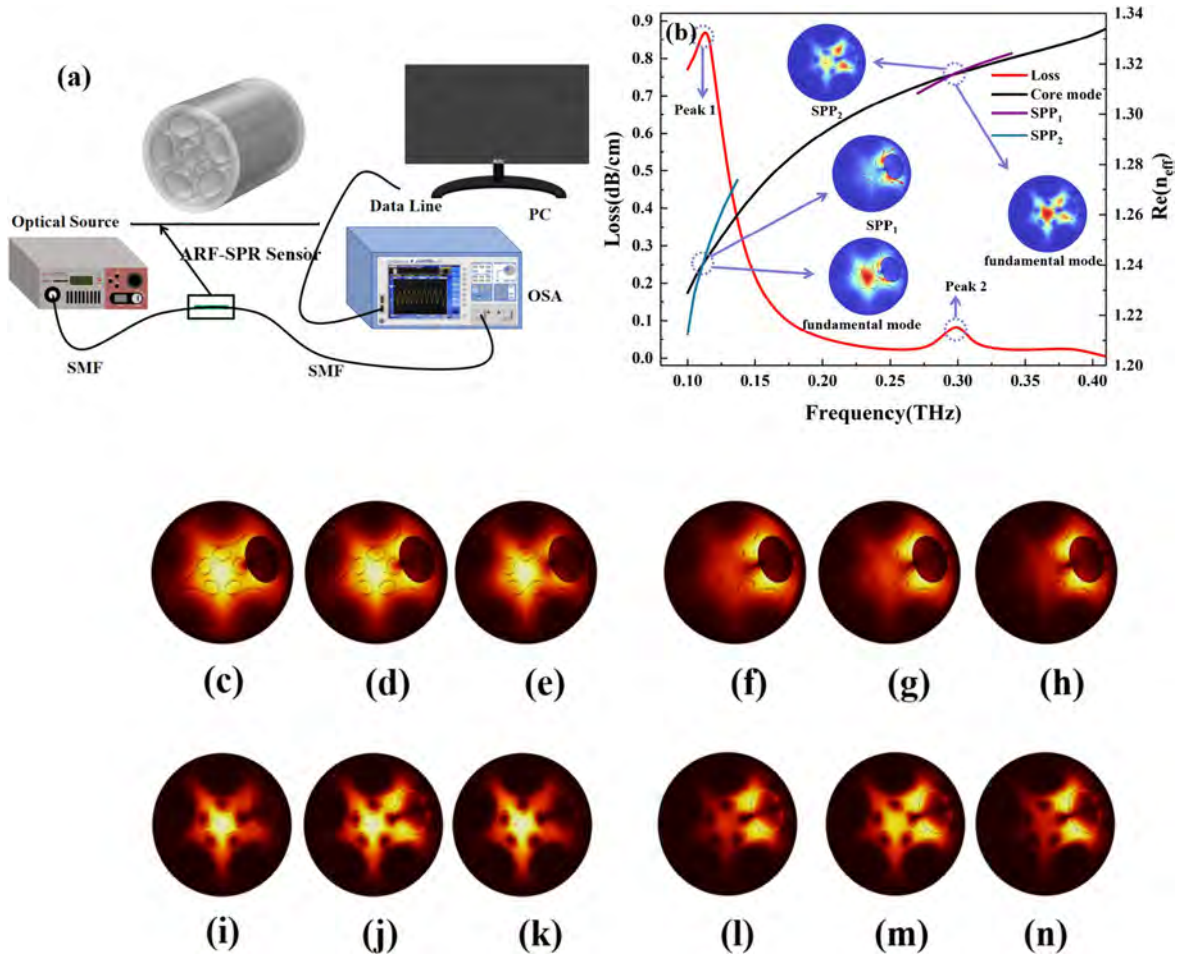

Fig. 5 **a** Schematic of the detection process of the ARF-SPR sensor; **b** dispersion relationship; mode field distributions: **c**–**h** Fundamental modes at frequencies of 0.1 THz, 0.113 THz, and 0.3 THz; **i**–**n** SPP modes at frequencies of 2.8 THz, 3.0 THz, and 3.2 THz

$$S(\lambda_{\mathrm{n}}) = \frac{\Delta\lambda_{\mathrm{n}_{peak}}}{\Delta n_{\mathrm{a}}} \tag{11}$$

$$S(\lambda_{\mathrm{T}}) = \frac{\Delta\lambda_{\mathrm{T}_{peak}}}{\Delta T} \tag{12}$$

where $\Delta\lambda_{\mathrm{n_{peak}}}$ and $\Delta\lambda_{\mathrm{T_{peak}}}$ are the variations of the resonance wavelengths of neighboring RIs and temperature, and Δn_{a} and ΔT are the adjacent RI and temperature changes, respectively. Figure 6(a) shows the loss curves for different RIs in the range of 1.30–1.36. With the change of RI, the two resonance peaks are significantly displaced and the resonance curves show similarity. However, at different RIs, the wavelength sensitivity and electric field strength exhibited by ARF-SPR sensors are different due to different offsets in loss and resonant frequency. Fig 6(b) shows the corresponding wavelength sensitivities at different RIs. As the RI of the empty core-filled analyte increases, the RI difference between the polymer Zonex and the liquid keeps decreasing, resulting in a partial transfer of photon energy from the core to the cladding tube. In addition, the RI difference between the cladding tube and the PDMS is smaller than the RI difference between the Zonex and the liquid, thus generating a swift field again at the interface between the inner wall of the tube and the PDMS, which interferes with the RI sensitivity of the ARF-SPR sensor. Since this interference is nonlinear, the RI sensitivity does not show a significant linear change with increasing RI of the analyte. As shown in Fig. 6(b-c) as RIs go up, the two resonance peaks tend to be closer together, while the resonance frequency of the first resonance peak blueshifts from 0.121 to 0.106 THz and that of the second resonance peak redshifts from 0.22 to 0.39 THz. The maximum wavelength sensitivities and average wavelength sensitivities of the first resonance peak and second resonance peak are 7057.50 μm/RIU / 13,888.9 μm/RIU and 5847.50 μm/RIU / 9906.76 μm/RIU, respectively. The resonance wavelengths of the two resonance peaks are linearly fitted:

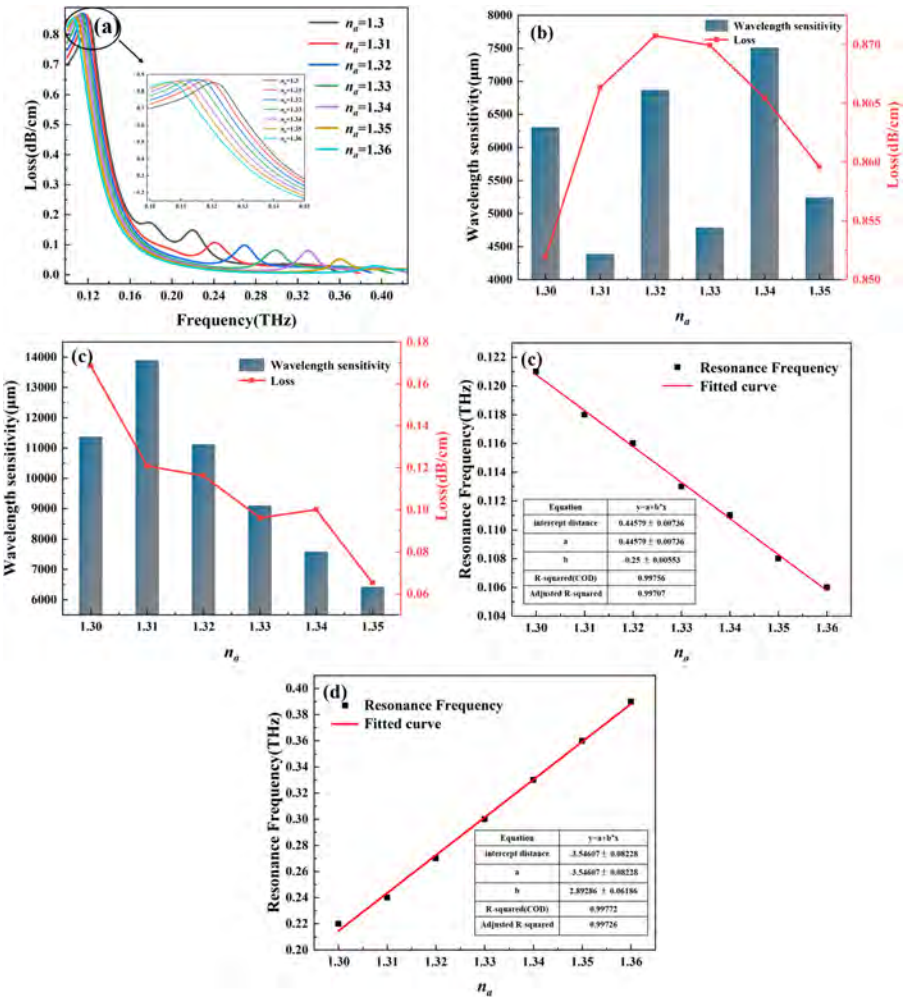

Fig. 6 **a** Loss spectra for $n_a = 1.30–1.36$; wavelength sensitivity and resonance frequencies: **b** first resonance peak and **c** second resonance peak; linear fitting of the resonance frequencies: **d** first resonance peak and **e** second resonance peak

$$\lambda_1 = 0.45 - 0.25n_a \tag{13}$$

$$\lambda_2 = -3.46 - 2.95n_a \tag{14}$$

where λ_1 and λ_2 are the resonance wavelengths of the two resonance peaks, respectively, and n_a is the RI of the analyte. As shown in Fig. 6(d-e) the corresponding R^2 of the two resonance peaks are 99.76% and 99.78%, and R^2 indicates that the sensor delivers excellent refractive index detection performance. We evaluated the sensor performance in the RI range of 1.30–1.36, covering the RIs of many essential biological agents and biochemical solutions, such as water (1.33), plasma (1.36), leukocytes (1.36), urinary solubility (1.341–1.3464), human intestinal mucosa (1.329–1.338), and glucose solution in water (10% solution = 1.3477, 20% solution = 1.3635). The designed sensor structure shows excellent sensing sensitivity and high resolution, thus providing a compact, label-free and convenient solution for biomedical liquids in the THz band [47].

Temperature

The temperature-sensitive material, PDMS, is introduced to the outer tube coated with graphene. As the RI of PDMS changes with temperature, the resonance peaks shift. Fig. 7(a) shows the loss curves of the two resonance peaks at different temperatures. When the temperature goes up from 26.85 to 76.85 °C, the resonance frequency of the first resonance peak does not change, whereas the resonance frequency of the second resonance peak redshifts from 0.222 to 0.285 THz and the loss peak exhibits a slightly decreasing trend. This is because the refractive index of PDMS decreases linearly with increasing temperature, leading to diminished resonance. As shown in Fig. 7(b-c) the maximum wavelength sensitivity and average wavelength sensitivity of the second resonance peak are 8.41 μm/°C and 5.97 μm/°C, respectively. The linearly fitted relationship between the temperature and resonance wavelength is represented by Eq. (15):

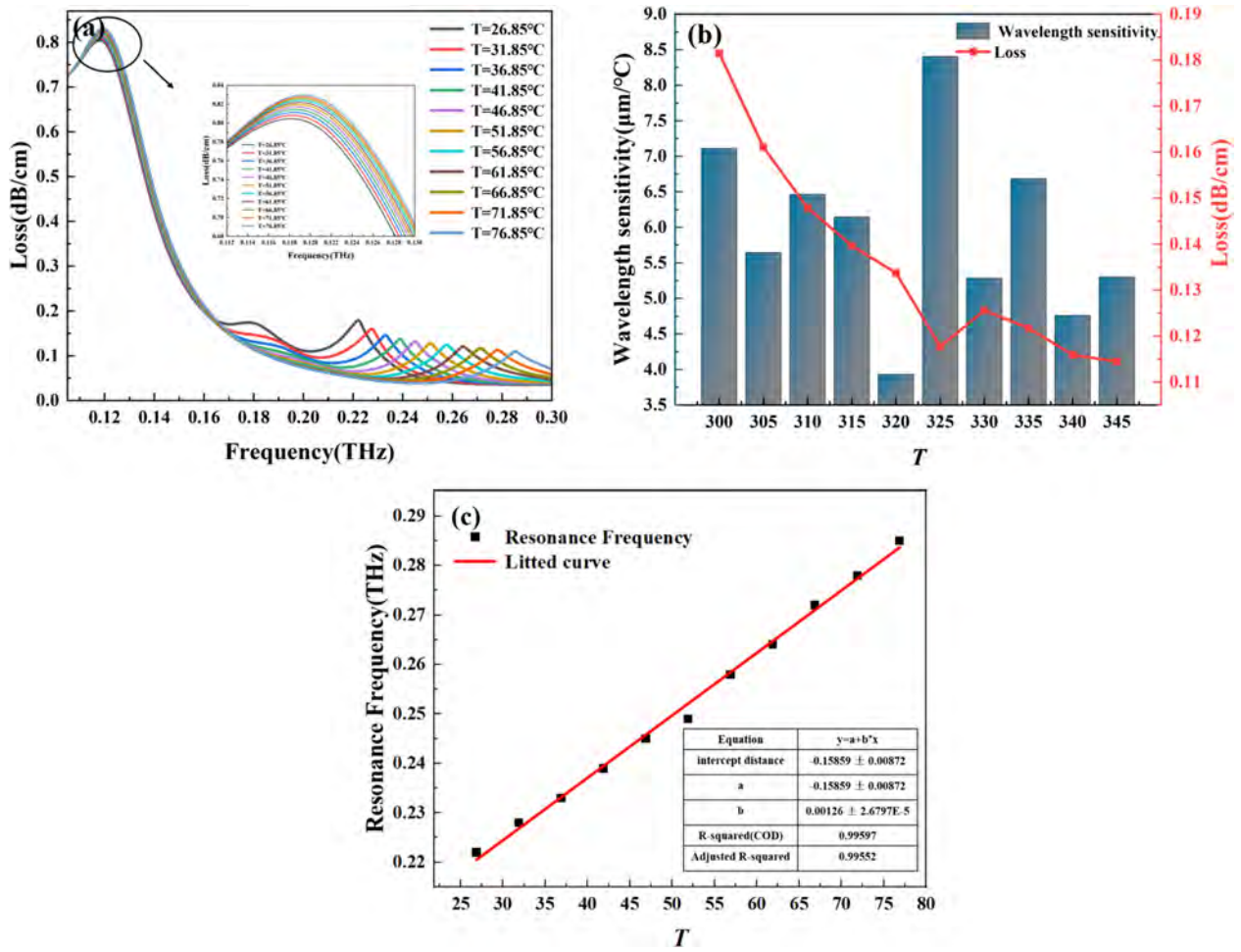

Fig. 7 (**a**) Loss spectra for T from 26.85 to 76.85 °C; (**b**) wavelength sensitivity and resonance frequencies of the second resonance peak: (**c**) linear fitting of the resonance frequencies of the second resonance peak

$$\lambda_2 = -0.15 + 1.29 \times 10^{-3} T \tag{15}$$

where λ_2 is the resonance wavelength of the second resonance peak, T is the temperature, and R^2 is 99.60%. According to the two-parameter measurement matrix given in Eq. (9), the RI and temperature detected by the ARF-SPR sensor can be demodulated by Eq. (16)

$$\begin{pmatrix} \Delta n \\ \Delta T \end{pmatrix} = \begin{pmatrix} 7057.5 & 0 \\ 13,888.9 & 8.41 \end{pmatrix}^{-1} \begin{pmatrix} \Delta\lambda_1 \\ \Delta\lambda_2 \end{pmatrix} \tag{16}$$

FOM and Resolution

Another important parameter is resolution. The lower the resolution, the more sensitive is the sensor. It is expressed by Eq. (17) [48]:

$$R = \frac{\Delta\lambda_{\min}}{S(n)} \tag{17}$$

where $S(n)$ is the wavelength sensitivity and $\Delta\lambda_{\min}$ is the minimum measurement by the spectrum analyzer (OSA). Regarding the detection of refractive indexes, the minimum resolution of the first and second resonance peaks are 1.33×10^{-8} RIU^{-1} and 7.2×10^{-9} RIU^{-1}, respectively, while for the detection of temperature, the second resonance peak has a minimum resolution of 1.19×10^{-5} RIU^{-1}. The second resonance peak thus shows superior detection ability than the first resonance peak.

The figure of merit (FOM) reflects the overall performance of the ARF-SPR sensor and is expressed by Eq. (18) [49]:

$$FOM = \frac{S(n)}{FWHM} \tag{18}$$

where FWHM is the full-width at half-maximum. In the refractive index range of 1.30–1.36, the maximum FOM

Table 1 Comparison of the properties of different sensors

Refs	*Structures*	*Films*	*Operating bands*	*Ranges*	*Wavelength sensitivity (μm/RIU)*
[50]	D-shape PCF	Graphene	0.45–0.75 THz	1.0–1.4 (RI)	305.5 μm/RI (avg.)
[18]	D-shape PCF	PVDF	200–300 μm	1.32–1.45 (RI)	335 μm/RIU
[51]	PCF	PVDF	280–320 μm	1.0–1.01 (RI)	400 μm/RIU
[17]	D-shape PCF	MoS2	1.0–2.0 THz	1.33–1.40 (RI)	715 μm/RIU
This work	ARF-PCF	Graphene/PDMS	0.1–0.4 THz	1.30–1.36 (RI) 26.85–76.85 ℃	13,888.9 μm/RIU 8.4 μm/℃

values of the first and second resonance peaks are 10.7 RIU^{-1} and 158 RIU^{-1}, respectively. The maximum FOM of the second resonance peak is less than 1 RIU^{-1} for temperature variations from 26.85 to 76.85 °C. The second resonance peak likewise is superior to the first resonance peak.

Comparison of Properties

The ARF-SPR sensor realizes dual-parameter measurements in the terahertz band, which is rarely accomplished so far. As shown in Table 1, the structure of this ARF is simpler. In terms of sensing performance, it is capable of detecting refractive index and temperature with higher wavelength sensitivity and resolution on the order of 10^{-8}.

Conclusions

A two-parameter ARF sensor is designed and analyzed. A negative curvature tube coated with graphene is combined with temperature-sensitive PDMS to realize dual measurements of the RI and temperature of external liquids in the 0.1–0.4 THz range. By constructing and demodulating the sensing matrix, the cross-sensitivity problem caused by the dual parameters is overcome. The inner tube radius ratio, outer tube radius ratio, and tube wall thickness are optimized by the finite element analysis. The results reveal that the average wavelength sensitivities of the first resonance peak and second resonance peak in the RI range of 1.30–1.36 are 5847.50 μm/RIU and 9906.76 μm/RIU, respectively. The resolution of the two resonance peaks is on the order of 10^{-8}, and the largest FOM is 158.14 RIU^{-1}. The average temperature sensitivity of the second resonance peak is 5.97 μm/°C, while the average resolution is 1.75×10^{-5} RIU^{-1} for temperature between 26.85 and 76.85 °C. This ARF-SPR sensor with excellent sensing sensitivity and high resolution has great application prospects in biosensing and other fields.

Author Contribution J.H. wrote the main manuscript text. J.W. involved in methodological research. L.X. participates in formal analysis. W.L. participates in data collation. J.L. participates in investigation. L.Y. participates in supervision. Q.L. participates in project administration. P.K.C. and C.L. participates in funding acquisition. All authors reviewed the manuscript.

Funding This work was jointly supported by the Heilongjiang Provincial Natural Science Foundation of China [JQ2023F001], National Natural Science Foundation of China [12304480], Local Universities Reformation and Development Personnel Training Supporting Project from Central Authorities, Natural Science Foundation of Heilongjiang Province [LH2021F007], China Postdoctoral Science Foundation funded project [2020M670881], City University of Hong Kong Strategic Research Grant (SRG) [7005505], and City University of Hong Kong Donation Research Grants [DON-RMG 9229021 and 9220061].

Data Availability Data sets generated during the current study are available from the corresponding author on reasonable request.

Declarations

Competing Interests The authors declare no competing interests.

References

1. Hasan MR, Akter S, Rifat AA, Rana S, Ali S (2017) A highly sensitive gold-coated photonic crystal fiber biosensor based on surface plasmon resonance. Photonics 4(1):18. MDPI
2. Sakib MN et al (2019) High performance dual core D-shape PCF-SPR sensor modeling employing gold coat. Results in Physics 15:102788
3. Liu C et al (2020) Surface plasmon resonance (SPR) infrared sensor based on D-shape photonic crystal fibers with ITO coatings. Optics Communications 464:125496
4. Lotfiani A, Ghanaatshoar M, Mohseni S (2019) Miniaturized optoelectronic SPR sensor based on integrated planar waveguide and MIM hot-electron photodetector. IEEE Trans Electron Devices 66(12):5215–5220
5. Rahad R et al (2024) A polarization independent highly sensitive metasurface-based biosensor for lab-on-chip applications. Measurement 114652
6. Rahad R et al (2023) Plasmonic refractive index sensing in the early diagnosis of diabetes, anemia, and cancer: an exploration of biological biomarkers. Results in Physics 49:106478
7. Harhouz A, Hocini A (2021) Highly sensitive plasmonic temperature sensor based on Fano resonances in MIM waveguide coupled with defective oval resonator. Opt Quant Electron 53(8):439
8. Liu W et al (2021) Surface plasmon resonance chemical sensor composed of a microstructured optical fiber for the detection of

an ultra-wide refractive index range and gas-liquid pollutants. Opt Express 29(25):40734–40747
9. Liu W et al (2023) Surface plasmon resonance sensor composed of microstructured optical fibers for monitoring of external and internal environments in biological and environmental sensing. Results in Physics 47:106365
10. Haque MA et al (2024) Numerical analysis of a metal-insulator-metal waveguide-integrated magnetic field sensor operating at sub-wavelength scales. Sensing and Bio-Sensing Research 43:100618
11. Haque MA et al (2023) Plasmonic sensor for rapid detection of water adulteration in honey and quantitative measurement of lactose concentration in solution. Results in Physics 51:106733
12. Chou Chao C-T et al (2021) Ultrahigh sensitivity of a plasmonic pressure sensor with a compact size. Nanomaterials 11(11):3147
13. Rahad R et al (2024) A novel plasmonic MIM sensor using integrated 1×2 demultiplexer for individual lab-onchip detection of human blood group and diabetes level in the visible to near-infrared region. IEEE Sensors J 24(8)
14. Sun S et al (2021) Investigation of mode couplings between core and cladding of terahertz anti-resonant fibres. J Phys D Appl Phys 54(18):185107
15. Zhang Y, Xue J, Zhang Y, Miao T, Yao Y, Wang Q, Gong J (2023) D-shaped terahertz microstructured fiber biosensor based on plasmon resonance on graphene surface. In: 2023 21st International Conference on Optical Communications and Networks (ICOCN). IEEE, pp 1–6
16. Wang D et al (2022) Tunable surface plasmon resonance sensor based on graphene-coated photonic crystal fiber in terahertz. Appl Opt 61(22):6664–6670
17. Liu S et al (2021) D-shaped surface plasmon resonance biosensor based on MoS2 in terahertz band. Opt Fiber Technol 66:102631
18. Zhang Y, Yao Y, Guang Z, Xue J, Wang Q, Gong J, Ali Z, Yang Z (2023) A high-sensitivity fiber biosensor based on PVDF-Excited surface plasmon resonance in the terahertz band. Photonics 10(10):1159. MDPI
19. Lv J et al (2022) Double-formant surface plasmon resonance for refractive index sensing by anti-resonance fibers with high sensitivity and wide detection range. Results in Physics 40:105876
20. Ankan IM et al (2020) Negative curvature hollow-core anti-resonant fiber for terahertz sensing. Appl Opt 59(28):8519–8525
21. Ni W et al (2021) Recent advancement of anti-resonant hollow-core fibers for sensing applications. in Photonics. MDPI
22. Sultana AS et al (2022) Nodeless antiresonant hollow core fiber for low loss flatband THz guidance. Optics Continuum 1(8):1652–1667
23. Li Y et al (2023) Surface plasmon resonance induced methane gas sensor in hollow core anti-resonant fiber. Opt Fiber Technol 78:103293
24. Mollah MA, Habib MS, Habib MS (2020) Novel hollow-core asymmetric conjoined-tube anti-resonant fiber for low-loss THz wave guidance. Osa Continuum 3(5):1169–1176
25. Kolyadin AN et al (2013) Light transmission in negative curvature hollow core fiber in extremely high material loss region. Opt Express 21(8):9514–9519
26. Paul AK et al (2021) Graphene-coated highly sensitive photonic crystal fiber surface plasmon resonance sensor for aqueous solution: Design and numerical analysis. in Photonics. MDPI
27. Rifat AA et al (2015) Photonic crystal fiber-based surface plasmon resonance sensor with selective analyte channels and graphene-silver deposited core. Sensors 15(5):11499–11510
28. Hanson GW (2008) Dyadic Green's functions and guided surface waves for a surface conductivity model of graphene. J Appl Phys 103(6)
29. Hanson GW, Yakovlev AB, Mafi A (2011) Excitation of discrete and continuous spectrum for a surface conductivity model of graphene. J appl phys 110(11)
30. Srivastava T, Purkayastha A, Jha R (2016) Graphene based surface plasmon resonance gas sensor for terahertz. Opt Quant Electron 48:1–11
31. Vasić B et al (2013) Tunable metamaterials based on split ring resonators and doped graphene. Appl Phys Lett 103(1)
32. Litchinitser N et al (2002) Antiresonant reflecting photonic crystal optical waveguides. Opt Lett 27(18):1592–1594
33. Mumtaz F et al (2022) A simple optical fiber SPR sensor with ultra-high sensitivity for dual-parameter measurement. IEEE Photonics J 14(5):1–7
34. Liu S et al (2016) Asymmetrically infiltrated twin core photonic crystal fiber for dual-parameter sensing. Opt Laser Technol 82:53–56
35. Feng Y et al (2023) Design and research of a dual-parameter photonic crystal fiber sensor. JOSA B 40(5):1267–1276
36. Liu C et al (2021) Overview of refractive index sensors comprising photonic crystal fibers based on the surface plasmon resonance effect. Chin Opt Lett 19(10):102202
37. Adamu AI et al (2021) Low-loss micro-machining of anti-resonant hollow-core fiber with focused ion beam for optofluidic application. Optical Materials Express 11(2):338–344
38. Debord B et al (2017) Ultralow transmission loss in inhibited-coupling guiding hollow fibers. Optica 4(2):209–217
39. Talataisong W et al (2021) Hollow-core antiresonant terahertz fiber-based TOPAS extruded from a 3D printer using a metal 3D printed nozzle. Photonics Research 9(8):1513–1521
40. Gao S-F et al (2016) Bending loss characterization in nodeless hollow-core anti-resonant fiber. Opt Express 24(13):14801–14811
41. Belardi W (2015) Design and properties of hollow antiresonant fibers for the visible and near infrared spectral range. J Lightwave Technol 33(21):4497–4503
42. Chen K et al (2019) Graphene photonic crystal fibre with strong and tunable light–matter interaction. Nat Photonics 13(11):754–759
43. Voiry D et al (2016) High-quality graphene via microwave reduction of solution-exfoliated graphene oxide. Science 353(6306):1413–1416
44. Sazio PJ et al (2006) Microstructured optical fibers as high-pressure microfluidic reactors. Science 311(5767):1583–1586
45. Wang Y et al (2021) Refractive index sensing and filtering characteristics of side-polished and gold-coated photonic crystal fiber with a offset core. Opt Laser Technol 136:106759
46. Zhang J et al (2022) A Surface plasmon resonance-based photonic crystal fiber sensor for simultaneously measuring the refractive index and temperature. polymers 14(18):3893
47. Islam MR et al (2020) Design of a fabrication friendly & highly sensitive surface plasmon resonance-based photonic crystal fiber biosensor. Results in Physics 19:103501
48. Shakya AK, Singh S (2021) Design of dual polarized tetra core PCF based plasmonic RI sensor for visible-IR spectrum. Optics Communications 478:126372
49. Islam MR et al (2022) Design of a dual cluster and dual array-based PCF-SPR biosensor with ultra-high WS and FOM. Plasmonics 17(3):1171–1182

50. Wang D et al (2023) D-Shaped photonic crystal fiber with graphene coating for terahertz polarization filtering and sensing applications. Opt Fiber Technol 103373
51. Hassani A, Skorobogatiy M (2008) Surface plasmon resonance-like integrated sensor at terahertz frequencies for gaseous analytes. Opt Express 16(25):20206–20214